



Cite this: *Mater. Adv.*, 2022, 3, 5430

Green and effective synthesis of gold nanoparticles as an injectable fiducial marker for real-time image gated proton therapy†

Haoran Liu, ^a Naoki Miyamoto, ^{bc} Mai Thanh Nguyen, ^a Hiroki Shirato^{cd} and Tetsu Yonezawa ^a

Fiducial markers are crucial for reducing damage to surrounding healthy tissues in real-time image gated proton therapy (RGPT) by boosting geometric accuracy and precision. This study aims to develop an injectable fiducial marker based on gold nanoparticles (Au NPs) synthesized by a green ethanol reduction method, as well as to determine the factors that affect their injectability and imaging capability. Au NPs synthesized in the ethanol-only system had an improved injectability (through 18 G and 21 G needles) and their imaging performance was almost identical to current fiducial markers used in the clinic. The reducing capacity of the ethanol system was significantly enhanced through the introduction of sodium alginate. Meanwhile, the addition of sodium alginate could also control the size of Au NPs, ranging from 21.8 to 14.1 nm. The product alg-Au NPs with smaller sizes enabled an injectability up to 100% even through 25 G needles with an extrusion force less than 17 N, which is superior for the injection of high-concentration Au NPs. A better imaging performance of alg-Au NPs was also verified in the X-ray visualization test. The work describes the green synthesis of Au NPs *via* the high-efficiency reducing system ethanol/alginate without the use of toxic reducing, capping, or stabilizing agents. The alg-Au NPs were found to exhibit promise as a fiducial marker for RGPT based on the injectability and imaging test.

Received 15th February 2022,
Accepted 16th May 2022

DOI: 10.1039/d2ma00172a

rsc.li/materials-advances

1. Introduction

The excellent biocompatibility, low toxicity, easy surface functionalization, and interactions between substances¹ of gold with different types of structures make them potential candidates in diverse biomedical fields,^{2,3} including clinical diagnostics,^{4,5} therapies,^{6,7} biosensors,⁸ and immunology.^{9,10}

^a Division of Materials Science and Engineering, Faculty of Engineering, Hokkaido University, Kita 13 Nishi 8, Kita-ku, Sapporo, Hokkaido 060-8628, Japan.

E-mail: tetsu@eng.hokudai.ac.jp

^b Division of Quantum Science and Engineering, Faculty of Engineering, Hokkaido University, Kita 13 Nishi 8, Kita-ku, Sapporo, Hokkaido 060-8628, Japan

^c Department of Medical Physics, Hokkaido University Hospital, Kita 14 Nishi 5, Kita-ku, Sapporo, Hokkaido 060-8648, Japan

^d Global Station of Quantum Medical Science and Engineering, Global Institution for Collaborative Research and Education, Hokkaido University, Kita 15 Nishi 7, Kita-ku, Sapporo, Hokkaido 060-8638, Japan

† Electronic supplementary information (ESI) available: Synthesis route of Au NPs, illustration of injectability test, schematic diagram of the X-ray visualization test, TEM of Au NPs, viscosities of sodium alginate solutions, visibility evaluation of samples with different gold amounts, TG of Au NP-based fiducial marker and alginate hydrogel, size distributions of Au NPs at different time points, UV-Vis spectra of Au NPs, TEM of sintered Au NPs at 600 °C, TEM, size distributions, average sizes and TG of alg-Au NPs after thermal treatment, visibility evaluation of alg-Au NPs, relationship between pattern matching scores of alg-Au NPs and TG of alg-Au NPs. See DOI: <https://doi.org/10.1039/d2ma00172a>

In addition to these applications, the unique properties of gold, *i.e.*, high atomic number, electron density, and surface plasmon resonance (SPR), also allow gold-based materials to be readily used for labelling and imaging, such as computed tomography (CT),^{11,12} magnetic resonance imaging (MRI),¹³ nuclear imaging,¹⁴ optical imaging,¹⁵ and photoacoustic imaging.¹⁶ For example, gold-based fiducial markers are essential in real-time image gated proton therapy (RGPT).^{17–19} By identifying the fiducial marker with X-ray beams, RGPT can accurately track the position of a tumour to avoid geometric uncertainties caused by breathing motion, peristalsis, and other body motions during therapy. As a result, RGPT is capable of improving the precision of radiation delivery, reducing the doses to the surrounding healthy tissues, and eventually achieving an optimal therapeutic efficacy and minimum treatment toxicity. However, currently used fiducial markers with large physical dimensions would lead to complicated and invasive insertion procedures, inducing undesired complications.^{20–22} Obviously, injectable fiducial markers based on smaller-sized gold nanoparticles (Au NPs) are promising and preferred in RGPT to relieve patients' pain and improve their clinical experience (Fig. 1).^{12,23–25}

For the synthesis of Au NPs, fabrication methods can be categorized into two types: top-down and bottom-up approaches. Top-down approaches generally involve the synthesis of Au NPs



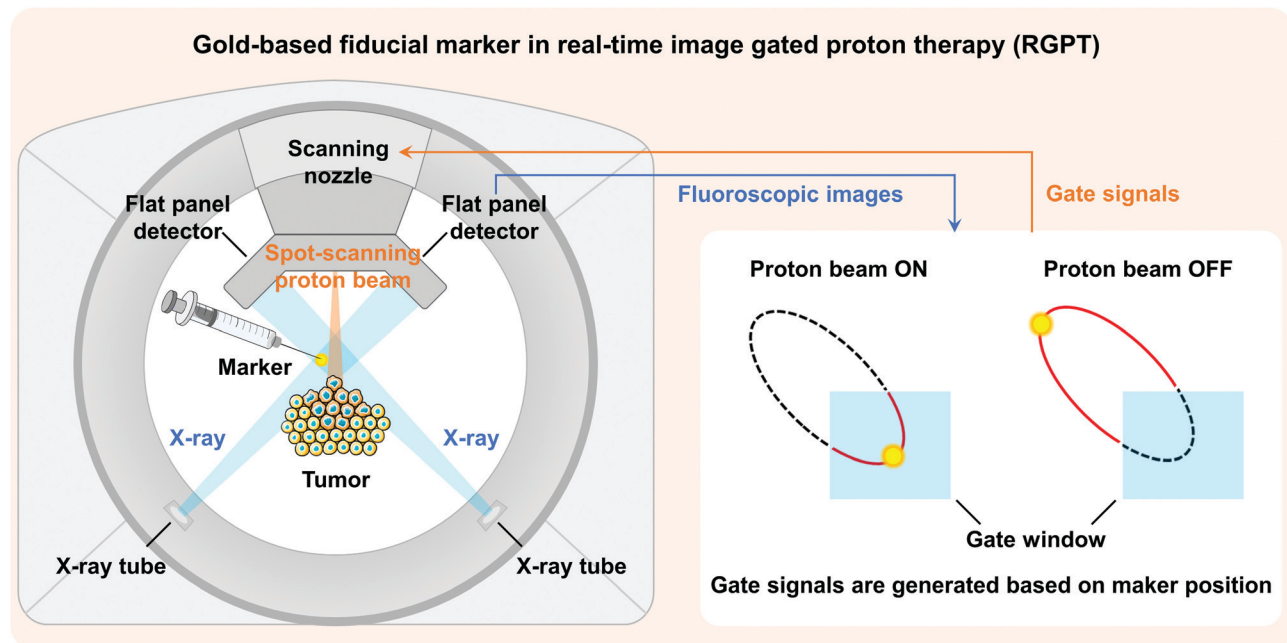


Fig. 1 Illustration of a gold-based fiducial marker in RGPT.

starting from bulk materials to nanoscale architectures using various methods, such as laser ablation,^{26,27} sputtering,²⁸ irradiation,²⁹ aerosol technology,³⁰ or lithography.³¹ However, top-down approaches are more susceptible to defects as the size becomes smaller and more expensive compared to bottom-up approaches.³² Conversely, bottom-up approaches begin by forming structures at the atomic level. Of all the bottom-up approaches for synthesizing Au NPs, the chemical reduction methods³³ are the most used strategies, while the Turkevich's method is the most classic and highly used chemical reduction technique for biomaterials,³⁴ in which gold ions in the precursor are reduced by reducing agents such as citrate,^{35,36} amino acid,³⁷ ascorbic acid,³⁸ or sodium borohydride.^{39,40} However, by-products may be generated by these agents during reactions and cause unexpected biological toxicity.⁴¹ For example, the presence of sodium citrate residues was proved to affect the proliferation and induce cytotoxicity in cells.^{42,43} Washing *via* centrifugation or water treatment is therefore indispensable.^{44,45} Furthermore, a highly controllable process protocol (temperature, reagent concentrations, and pH) must be strictly followed in order to synthesize monodisperse Au NPs with desired sizes.⁴⁶ Instead, a low carbon-number alcohol reduction method was pioneered to synthesize noble metal NPs as catalysts for hydrogenations.^{47–49} With the validated reduction capacity for mono- and bimetallic NP synthesis,^{50–52} as well as its environment-friendly and non-toxic properties, the alcohol reduction method represents a green alternative for manufacturing Au NPs.

In this work, a facile, green, and biocompatible preparation method based on the ethanol reduction system to prepare Au NPs for fiducial marker application was demonstrated. Initially, Au NPs were synthesized in the ethanol-only system and their injectability and imaging capabilities as fiducial markers were evaluated. The synthesized Au NPs had an improved injectability

(through 18 G and 21 G needles) and an almost identical imaging capability compared to the current fiducial markers used in the clinic. Due to the mild reducing capacity of ethanol and the lack of stabilizing agents, challenges such as low reaction rate, aggregation, and relatively large size were still faced in the preparation of Au NPs and further injection through thinner needles (25 G). Sodium alginate is a natural polymer with excellent biocompatibility and low toxicity. Owing to the abundant free hydroxyl and negatively charged carboxyl groups, alginate has the potential to accelerate the reaction rate and control the growth of Au NPs, which is supported by our previous work.³ For this reason, the strategy of adding sodium alginate to the ethanol system was explored to tackle these limitations for higher efficacy and improved injectability. The reducing capacity of the ethanol system was significantly enhanced because of the introduced hydroxyl and carboxyl groups distributed along the alginate backbone.⁵³ Moreover, the size of synthesized Au NPs prepared in the presence of sodium alginate (alg-Au NPs) could be regulated by the alginate chain-formed cavities and the increased nucleation probability. The average sizes of alg-Au NPs synthesized in different concentrations of alginate (0.1, 0.5, 0.7% w/v) were 21.8 ± 5.1 , 18.2 ± 3.0 , and 14.1 ± 3.5 nm, respectively. Au NPs with a smaller size enabled a superior injectability up to 100% even through 25 G needles with an extrusion force of less than 17 N. As a result of the increased gold surface area and more Au NPs distributed in the path of X-ray transmission, alg-Au NPs showed a better imaging performance with the same gold concentration. Within the range of parameters studied, the viscosities of injection media, Au NP concentrations, and needle gauges were found to be the major factors that would affect their injectability, while the gold amount and particle size dominated their imaging performance. The results of this work validate a green and high efficiency

reducing system and the potential of synthesized Au NPs as a fiducial marker for real-time image gated proton therapy.

2. Experimental section

2.1. Materials

Tetrachloroauric(III) acid hydrate ($\text{HAuCl}_4 \cdot n\text{H}_2\text{O}$, $n = 3.7$, Kojima, Japan), sodium alginate (alg, I-8, Kimica Corp., Japan), and anhydrous ethanol (Wako, compliant with Japanese Pharmacopoeia) were used as a precursor, an additive, and a reducing agent, respectively. 1 g of $\text{HAuCl}_4 \cdot n\text{H}_2\text{O}$ ($n = 3.7$) was dissolved in 100 mL of pure water to obtain a 24.6 mM aqueous solution of HAuCl_4 . All chemicals were used as received. The pure water (Organo Puric system, $> 18.2 \text{ M}\Omega \text{ cm}$) was used to prepare solutions. Injection of Au NPs was carried out using 1 mL plastic syringes with a diameter of 4.2 mm and a length of 104 mm.

2.2. Preparation of Au NPs and alg-Au NPs

As shown in Fig. S1, (ESI[†]) to prepare Au NPs, 191.9 mL pure water and 200 mL ethanol were mixed into a 1 L two-necked flask and were heated in an oil bath. An 8.1 mL aqueous solution of HAuCl_4 (24.6 mM) was added when the mixed solution boiled. The reaction solution was kept for 2 h under reflux and stirred at 800 rpm. When the reaction was completed, the products were collected after a 10-minute water-cooling and ultrasonic process. In order to prepare alg-Au NPs, pure water was replaced with an equal volume of sodium alginate aqueous solution and the concentrations of the original sodium alginate aqueous solutions were 0.1, 0.5, and 1.0% w/v. The obtained alg-Au NPs were labelled with the original alginate concentrations: 0.1, 0.5, and 1.0% w/v. In Section 3.2.2, ethanol was replaced with an equal volume of pure water to obtain an alginate-only system to synthesize Au NPs. The Au NPs were still labelled with original alginate concentrations.

2.3. Characterizations

UV-Vis spectra were collected to observe Au NP formation by using a UV-Vis spectrophotometer (UV-1800, Shimadzu) and a quartz cell with a 1 cm optical path. Transmission electron microscopy (TEM, JEOL JEM-2000-FX, at 200 kV) was used to analyse the morphology and size of alg-Au NPs. For TEM sample preparation, dispersions of Au NPs or alg-Au NPs were placed on collodion film-coated copper TEM grids and left for natural drying. Thermogravimetric (TG, DTA-60H, Shimadzu) analysis was carried out to confirm the mass ratio of gold to sodium alginate and to evaluate the thermal decomposition behaviour of samples. Fourier-transform infrared (FT-IR) spectroscopy (Nicolet IS10, Thermo Fisher Scientific) was employed to analyse the functional groups of alginates before and after reactions in the range of 4000–500 cm^{-1} . The viscosities of sodium alginate aqueous solutions with different concentrations were measured by a viscometer (DV-I Prime, Brookfield) with shear rate sweeps from 4.0 to 200.0 s^{-1} at room temperature.

2.4. Injectability tests

The injectability was evaluated by extraction forces and injectability ratios with an Automatic Vertical Servo Stand (JSV H1000, Algol Instrument). Briefly, as illustrated in Fig. S2 (ESI[†]), samples were loaded into a 1 mL syringe with an 18 G (inner diameter: 0.84 mm φ), 21 G (inner diameter: 0.51 mm φ), or 25 G (inner diameter: 0.26 mm φ) needle. The minimum forces to inject all samples (injectability: 100%) were recorded. The volume percentage of the extruded sample with respect to the total sample under a force of 50 N was defined as injectability. The threshold of the experimental platform was set to 70 N and the instrument would stop when the extraction force exceeded 70 N.

2.5. X-Ray visualization tests

In order to evaluate the X-ray visualization of samples, the X-ray visualization tests were conducted at the Central Institute of Isotope Science, Hokkaido University. Fig. S3 (ESI[†]) shows the schematic diagram of the X-ray visualization test. The samples were injected into jelly and then were taken out and irradiated with X-rays generated from an X-ray tube (UD-150-B40, Shimadzu). Gold ball markers (99.99% Au) with diameters of 1.5 and 2.0 mm were chosen as the control. The size and shape of the marker were determined to be suitable for pattern recognition during marker tracking.⁵⁴ The X-rays passed through the samples would be detected by the Flat Panel Detector (PaxScan 3030, Varian Medical System). Besides, acrylic resins that have an X-ray attenuation property close to the human body were placed between the samples and the detector,⁵⁵ and the visualization ability was evaluated by the pattern matching scores quantified by the detector. The pattern matching scores were calculated according to a previous study.⁵⁶

3. Results and discussion

3.1. Au NPs synthesized via ethanol reduction as a fiducial marker

For various diagnostic and therapeutic applications, different types of reducing, capping, or stabilizing agents are required for the preparation of Au NPs with a desirable shape and size. Considering the *in vivo* usage scenarios of Au NPs and the potential toxicity of these agents, Au NPs were first synthesized via a one-step method using ethanol as a reducing agent in the present work.

3.1.1. Preparation of Au NPs. First, the preparation and characterization of Au NPs prepared by the ethanol reduction method in pure water/ethanol mixed solvent without any stabilizing molecules is reported. Fig. 2(a) shows the UV-Vis extinction spectrum of Au NPs. The spectrum of Au NPs exhibited a surface plasmon resonance (SPR) peak with a maximum absorption wavelength (λ_{max}) at around 576 nm. Furthermore, another two SPR peaks centred at 738 and 833 nm were attributed to large hexagonal Au NPs, as evidenced by the TEM images in Fig. 2(b) and Fig. S4 (ESI[†]). When reductions occur on the surface of Au nucleated seeds, they depend on the surface energy of the different crystal facets.



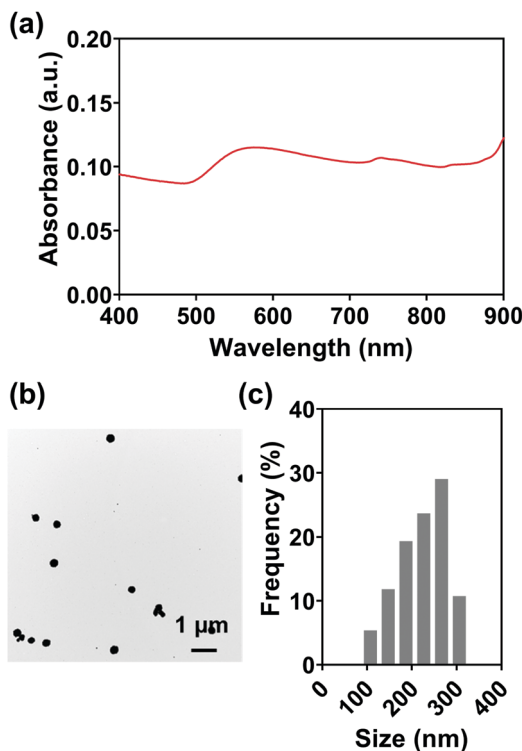


Fig. 2 (a) UV-Vis spectrum, (b) TEM image, and (c) size distribution (taken from TEM image) of Au NPs prepared via an ethanol reduction method in pure water/ethanol mixed solvent without any stabilizing molecules.

Therefore, polygonal particles would be generated during the reduction process.⁵⁷ Fig. 2(c) shows the size distribution of Au NPs obtained from the arbitrarily chosen area of enlarged TEM images and their average size is approximately 242.5 ± 55.4 nm.

3.1.2. Injectability of Au NPs. High-efficiency transfer of Au NPs through injection guarantees superb image quality and the high injectability of fiducial markers is a key factor in improving patients' clinical experience by relieving pain during insertion procedures. Therefore, it is critical to study the injectability of Au NPs and to investigate the effects of relevant parameters (*i.e.*, the viscosity of injection medium, Au NP concentration, and needle gauge) on injectability.

An aqueous solution of sodium alginate was selected as an injection medium in this work for its advantages such as ease of preparation, biocompatibility, biodegradability, and nontoxicity.⁵⁸ And the effect of injection medium viscosity (adjusted by altering alginate concentration, Fig. S5, ESI[†]) on injectability was firstly evaluated as the viscosity is vital for the efficient delivery of Au NPs and their uniform distribution in the injection medium. Fig. 3(a) shows the extrusion forces required for different concentrations of alginate aqueous solutions (1.0, 2.5, 5.0% w/v) as injection media. Extrusion force curves are normally characterized by a very rapid increase of the force followed by a steady stage. The average extrusion forces of steady stages are exhibited in Fig. 3(b). When the concentration of alginate aqueous solution was 1.0% w/v, the extrusion forces for 100% injectability were 0.7 N for an 18 G needle, 0.8 N for a 21 G needle, and 4.4 N for a 25 G needle. When the alginate concentration increased to 2.5% w/v, the extrusion

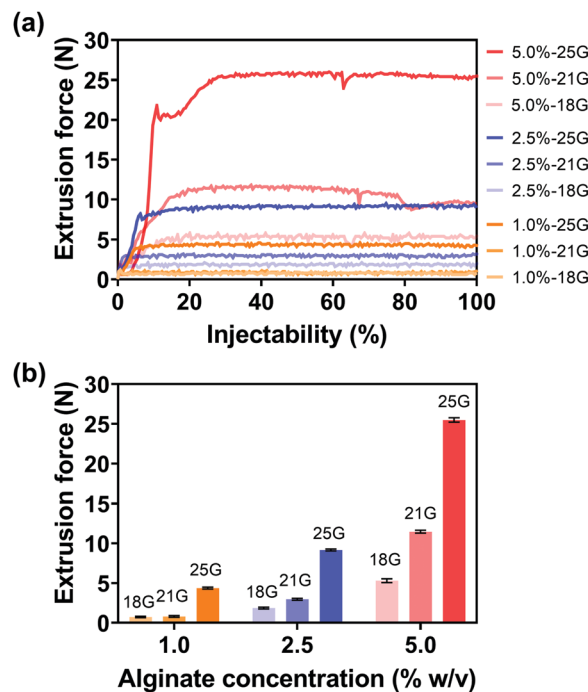


Fig. 3 (a) Extrusion force curves and (b) average extrusion forces of injection media with different concentrations of aqueous solutions of sodium alginate when passing through different gauge needles.

forces increased to 1.8, 3.0, and 9.2 N for the 18 G, 21 G, and 25 G needles, respectively. A further 2-fold increase in alginate concentration (5% w/v) caused increases in extrusion forces to 5.3, 11.5, and 25.5 N for 18 G, 21 G, and 25 G needles, respectively. The extrusion force required for injection is generally dissipated in three ways: (a) overcoming the resistance force between the syringe and plunger, (b) imparting kinetic energy to the injection medium, and (c) forcing the injection medium through the needle.^{59,60} The kinetic energy contributes to the flow of the injection medium while the driving force pushes the injection medium through the needle. Therefore, larger extrusion forces are needed for high-viscosity injection media and needles with smaller inner diameters.

After the introduction of Au NPs, the kinetic energy increased since the motion of contained Au NPs was driven by the injection medium and required additional kinetic energy. On the other hand, due to potential congestion and clogging of Au NPs in the needle, the driving force of the injection media with Au NPs also increased. Consequently, the introduction of Au NPs into the injection medium would increase the kinetic energy and driving force of the injection medium, which would further increase the extrusion force. Therefore, the Au NP concentration is another important parameter that will strongly influence the injectability. In addition, the Au NP concentration is also the key factor for imaging performance. Three different Au NP concentrations (0.3, 0.5, and 0.7 g mL⁻¹) were consequently selected and evaluated for the balance of superior imaging performance and an extrusion force acceptable to the surgeon during injection. The extrusion forces were subsequently measured by altering the Au NP

concentrations in different viscosities of injection media through 18 G needles. The injection system was a physical mixture of Au NPs and sodium alginate aqueous solution. When using a low-viscosity sodium alginate aqueous solution (1.0% w/v, viscosity = 170.0 mPa s at a shear rate of 4 s⁻¹, Fig. S5, ESI[†]) as an injection medium, Au NPs would overcome the lateral drag force and precipitate, resulting in no injectability. Instead, the precipitation of Au NPs can be avoided since Au NPs cannot overcome the lateral drag force in high-viscosity sodium alginate aqueous solution (viscosities of 2.5 and 5.0% w/v sodium alginate solution are 9525 and 45244 mPa s at a shear rate of 4 s⁻¹, Fig. S5, ESI[†]). The uniform distribution of Au NPs in the injection medium and the subsequent injectability can be therefore guaranteed. The alginate concentrations of injection media 2.5 and 5.0% w/v were consequently determined for the next injection tests. Fig. 4(a) shows the extrusion forces of injection media with different concentrations of Au NPs. It was given by the red lines that the extrusion force surged when the Au NP concentration was 0.7 g mL⁻¹. High concentration Au NPs increased the possibility of NP accumulation, and Au NPs were more likely to clog in the needles during injection, resulting in soaring extrusion forces and injectability of less than 10%. In contrast, 100% injectability could be achieved at Au NP concentrations of 0.3 and 0.5 g mL⁻¹ (yellow and blue lines). Given that high concentration Au NPs can provide a better imaging performance, 0.5 g mL⁻¹ was preferred for the following measurements. In particular, with the same concentration of Au NPs, the higher concentration of injection medium needed a higher extrusion force (Fig. 4(b)), in agreement with the previous results (Fig. 3). However, when the Au NP concentration was 0.5 g mL⁻¹, the extrusion force for the injection medium with

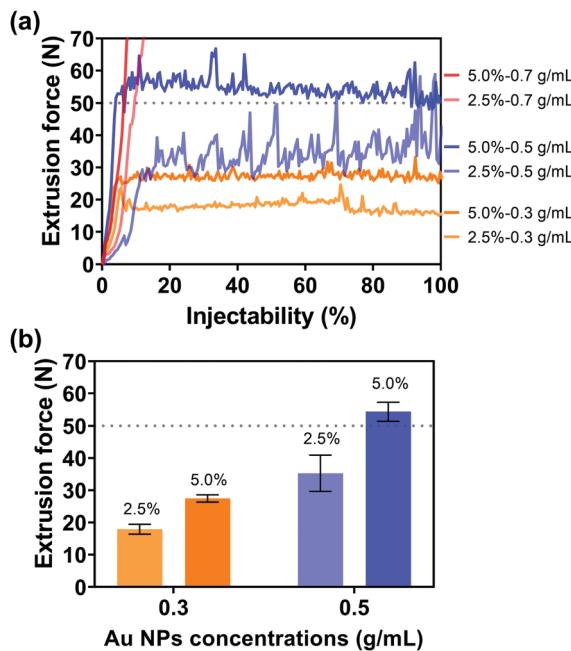


Fig. 4 (a) Extrusion force curves and (b) average extrusion forces of different concentrations of Au NPs (prepared by ethanol reduction in ethanol/water mixture without stabilizing molecules) of the injection medium with sodium alginate concentration. Needle gauge: 18 G.

5.0% w/v of alginate concentration exceeded 50 N (grey dashed line), which was not practical since 50 N is the maximum acceptable force for a surgeon to apply on a syringe during the injection.^{61,62} For this reason, although a high-concentration injection medium might facilitate the dispersion of Au NPs, the alginate concentration was ultimately determined to be 2.5% w/v.

In addition to the viscosities of the injection media and Au NP concentrations, the effect of needle gauges on injectability was also evaluated. Since the inner diameter of the 25 G needle (0.26 mm φ) was too small for highly concentrated Au NPs with an average particle size of 242.5 \pm 55.4 nm, no particles can flow through the needle, Fig. 5(a) only shows the extrusion forces of the injection medium (alginate concentration: 2.5% w/v) with Au NPs (Au NP concentration: 0.5 g mL⁻¹) through the 18 G and 21 G needles. The small diameter of the needles made the flow of the injection medium with Au NPs through the needle more difficult, as shown in Fig. 5(b), where one can see the average extrusion forces for the 18 G and 21 G needles were 34.1 and 41.9 N, respectively. Furthermore, a thin needle also potentially increased the chance of needle blockage, inducing a dramatic increase in extrusion force and a decrease in injectability, by approximately 83.5 and 66.9% for 18 G and 21 G needles.

3.1.3. Imaging performance. Following the injectability evaluation, the imaging performance of samples containing different gold amounts (#1–7) and clinically used gold ball markers (1.5 and 2.0 mm φ) was tested by the X-ray visualization test. Fig. 6(a) shows images obtained from an X-ray visualization

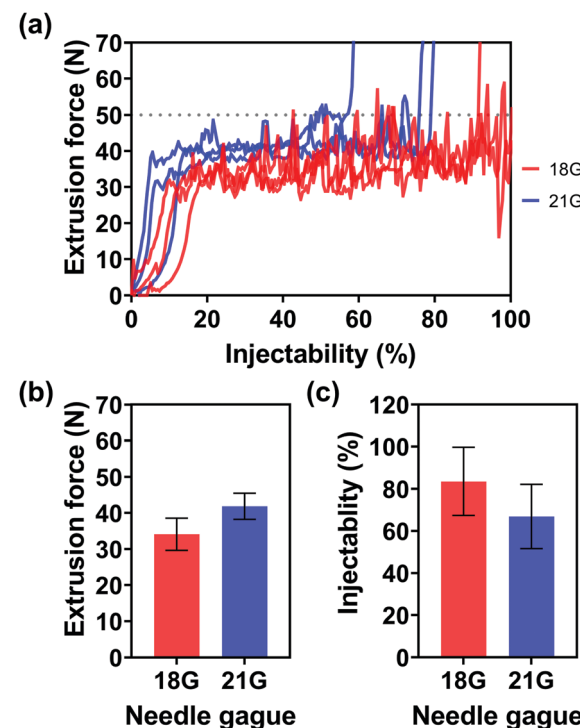


Fig. 5 (a) Extrusion force curves, (b) average extrusion force, and (c) injectability (ratio of injected volume/total volume with extraction force of 50 N) through different needle gauges. Injection medium: sodium alginate with a concentration of 2.5% w/v; Au NP concentration: 0.5 g mL⁻¹.



test under different acrylic resin thicknesses and tube currents. The pattern matching scores calculated based on these images are displayed in Table S1 and Fig. S6 (ESI[†]). The pattern matching score is a quantitative measurement of the visibility of the object, and the maximum score is defined as 100. Samples with a score over 30 are considered sufficiently visible. To intuitively compare the imaging performance of the Au NPs and gold ball marker, the pattern matching scores of Au NPs were normalized by dividing them by the pattern matching score of the 2.0 mm gold ball marker under the same acrylic resin thickness and tube current, and the gold amounts contained in samples were calculated based on their TG analysis, as exhibited in Fig. 6(b) and Fig. S7 (ESI[†]). Under a thin acrylic resin (10 cm), samples containing a small amount of Au NPs (15.00 mg) showed an acceptable imaging capability. However, the pattern matching scores decreased with increasing acrylic resin thickness, suggesting that the human tissue would also cause the attenuation of X-ray and affect the *in vivo* visibility of Au NPs as a fiducial marker. Higher pattern matching scores under thicker acrylic resin could be achieved by raising the tube current to improve their imaging performance deep inside the human body. For samples containing more gold, the higher gold amount also endowed them with enhanced imaging capability under thicker acrylic resins. In particular, sample #5 could reach a similar imaging level (all normalized pattern matching scores larger than 80%) with a smaller gold amount (29.87 mg) compared to the 2.00 mm gold ball marker (80.95 mg). These results demonstrate that the Au NPs synthesized *via* the ethanol reduction are capable of being a fiducial marker for an imaging application.

3.2. alg-Au NPs synthesized *via* ethanol reduction with alginate as the fiducial marker

Ethanol reduction is a green method for the synthesis of Au NPs without the addition of toxic reducing and stabilizing agents. However, the challenges of low reaction rate, excessive reaction-induced aggregation and precipitation, and the relatively large particle size still remain because of the mild reducing capacity of ethanol and the long reaction time. In particular, the aggregation

between Au NPs and their large size would further increase the risk of needle clogging during injections, leading to zero injectability through thin needles (25 G) and inefficient transfer through larger gauge needles (Fig. 5). Owing to the abundant free hydroxyl and carboxyl groups distributed along the backbone and interpenetrating chains after being dissolved in solution,⁶³ sodium alginate might have the potential to accelerate the reaction rate and control the growth of Au NPs. For this reason, sodium alginate was introduced into the green reduction system for high-efficiency synthesis of Au NPs with controlled particle sizes.

3.2.1. Synthesis of alg-Au NPs. As shown in Fig. 7(a), the formations of alg-Au NPs in different concentrations of alginate were confirmed by the UV-vis spectra, in which SPR peaks with λ_{max} around 535 nm could be observed. In comparison with the UV-vis spectrum of Au NPs synthesized in the ethanol-only system, the spectra of alg-Au NPs displayed an ideal bell shape, indicating that negligible aggregation occurred, and the Au NPs were well dispersed. Moreover, according to the spectra, there were only single SPR peaks around 535 nm, which indicates that very few hexagonal or triangular Au NPs were generated in the ethanol/alginate system. This could also be verified by their TEM images.

Fig. 7(b) shows the TEM images and their size distributions of Au NPs synthesized in the ethanol/alginate system with various alginate concentrations and most alg-Au NPs were spherical. Meanwhile, in Fig. 7(c), the decreasing particle size of alg-Au NPs with the increasing alginate concentration can be observed based on their particle size distributions. The cavities formed by alginate chains could serve as a template to limit the uncontrollable growth of Au NPs. As a result, Au NPs synthesized in a higher concentration of alginate aqueous solutions would have a smaller particle size. The size of Au NPs is critically important to their properties and biomedical applications, including biodistribution,⁶⁴ metabolism,⁶⁵ permeation,⁶⁶ cytotoxicity,⁶⁷ and cell uptake.⁶⁸ Radiosensitization,⁶⁹ X-ray attenuation,⁷⁰ and targeted delivery⁷¹ are also size-dependent. Therefore, in addition to reducing the risk of needle clogging, the use of Au NPs can also be extended to other biomedical

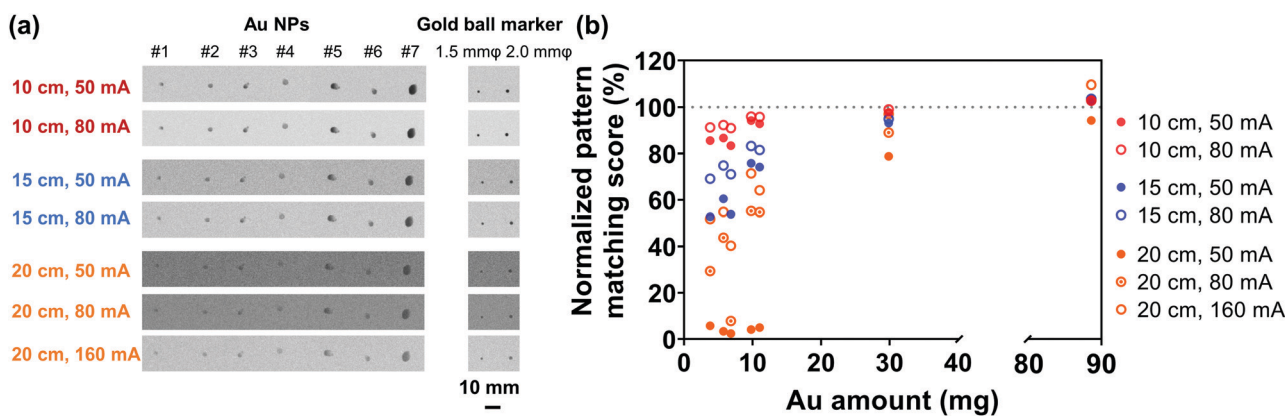


Fig. 6 (a) X-Ray visualization image of gold ball markers and samples with different amounts of Au NPs under different acrylic resin thicknesses and tube currents. (b) Relationship between normalized pattern matching scores and different gold amounts.



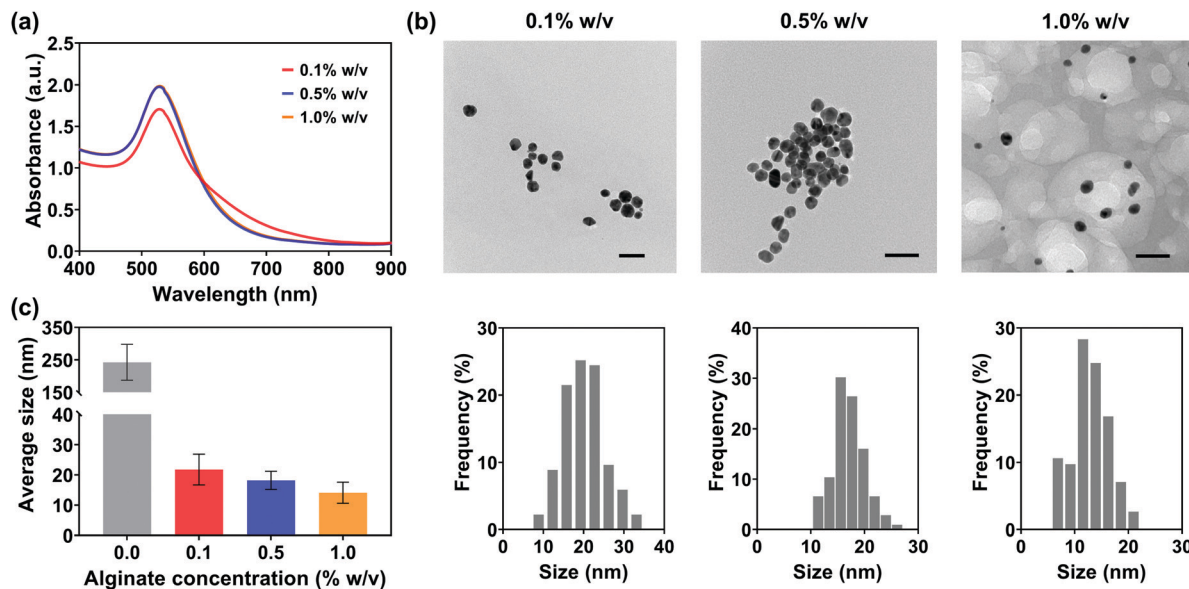


Fig. 7 (a) UV-Vis spectra, (b) TEM images and size distributions, and (c) average sizes of alg-Au NPs prepared with different alginate concentrations. The scale bars shown in all TEM images indicate 50 nm.

applications by controlling the size of Au NPs *via* regulating the alginate concentration.

3.2.2. Formation of alg-Au NPs in the ethanol/alginate system. As expected, the addition of alginate was capable of facilitating the reduction reaction, as validated by the start time of the reaction (the time when the solution colour changed) in Fig. 8. The reaction almost started immediately when the alginate concentration was 1.0% w/v, exhibiting the excellent reducing capacity of the ethanol/alginate system. Even though the alginate concentration decreased to 0.1% w/v, the start time of the reaction was still shorter than that of the ethanol-only system, which normally required at least 1 h for the formation of Au NPs. In order to investigate the formation process of Au NPs in the ethanol/alginate system, Au NPs synthesized with 0.5% w/v alginate aqueous solutions were collected at different time points for further characterizations.

In Fig. 9(a), the SPR peak of Au could be observed at 30 s, which confirmed the formation of Au NPs. Thereafter, the

absorption intensity increased with reaction time and reached a relatively stable level after 60 s. Remarkably, the absorption intensity at 150 s was almost the same as the intensity after 2 h. These UV-vis spectra clearly demonstrate that Au NPs formed within 30 s in the ethanol/alginate system and the reaction from Au(III) to Au(0) was basically completed after 150 s.

Fig. 9(b) and Fig. S8 (ESI†) represent the TEM images and their size distributions of Au NPs at different time points, and their average sizes are shown in Fig. 9(c). The average sizes of the synthesized Au NPs did not change significantly at different time points and were all around 18 nm, suggesting that the chain-like structure and formed cavities can indeed limit the growth of Au NPs and prevent them from aggregation and precipitation induced by the long reaction time. Furthermore, the coefficient of variation (CV) of Au NPs (Fig. 9(d)), which is defined as the ratio of their standard deviation to the average size, gradually decreased with reaction time, which implied that the size of Au NPs became more uniform as the reaction progressed.

The FT-IR spectra of sodium alginate and alg-Au NPs were measured to confirm if sodium alginate was involved in the reaction. As shown in Fig. 9(e), all FT-IR spectra show broad peaks at *ca.* 3500 cm⁻¹, which are attributed to the stretching of hydroxyl groups due to the presence of water. Low-intensity peaks at about 2900 cm⁻¹ are due to the -CH₂ groups. The absorption bands corresponding to the asymmetric and symmetric stretching modes of the carboxylate salt groups (-COONa) are located at 1610 cm⁻¹ and 1417 cm⁻¹. The absorption bands at 1304 cm⁻¹ are ascribed to the asymmetrical stretching of the C-O-C group while the vibrations in the range 1100–1000 cm⁻¹ correspond to the glycoside bonds in the polysaccharide (stretching C-O-C). Peaks at 946 cm⁻¹, 890 cm⁻¹, and 818 cm⁻¹ are attributable to the C-H vibration of the pyranose (ring of the alginate) group.⁷² By comparing the FT-IR spectra of sodium alginate and alg-Au

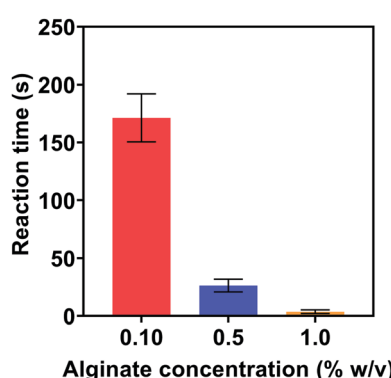


Fig. 8 Start time of the reactions in the ethanol/alginate systems with different concentrations of alginate.



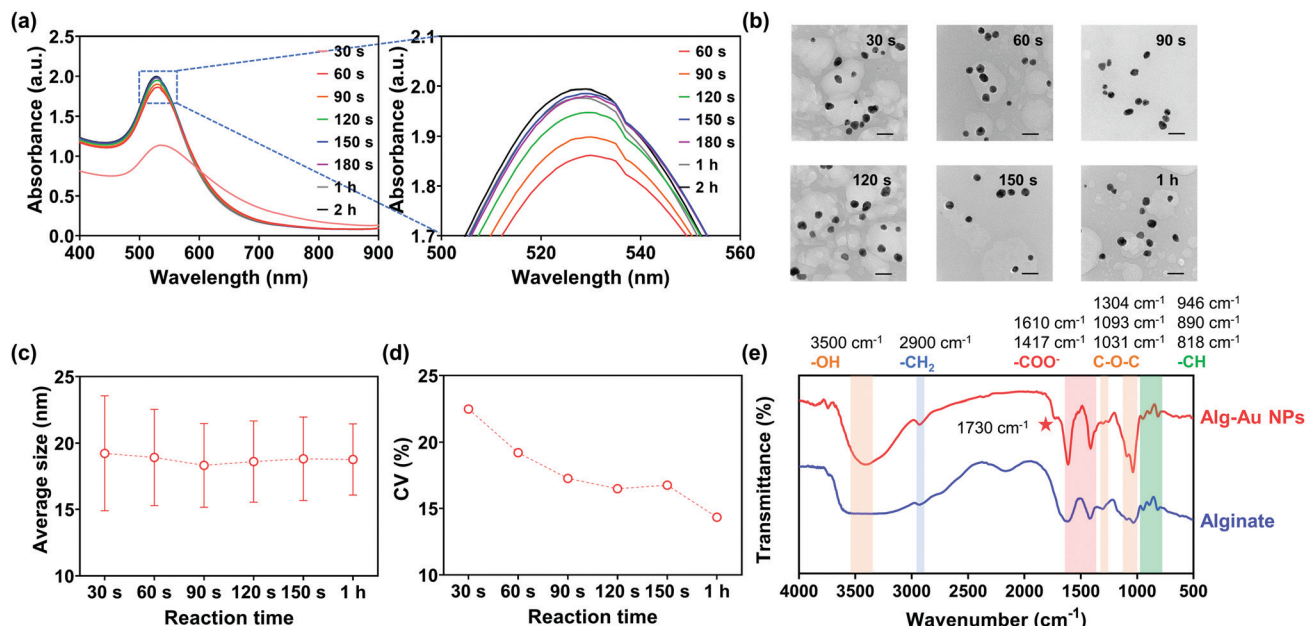


Fig. 9 (a) UV-Vis spectrum, (b) TEM, (c) average sizes, and (d) CV of alg-Au NPs synthesized with 0.5% w/v alginate aqueous solutions. (e) FTIR of alg-Au NPs and alginate. The scale bar is 50 nm.

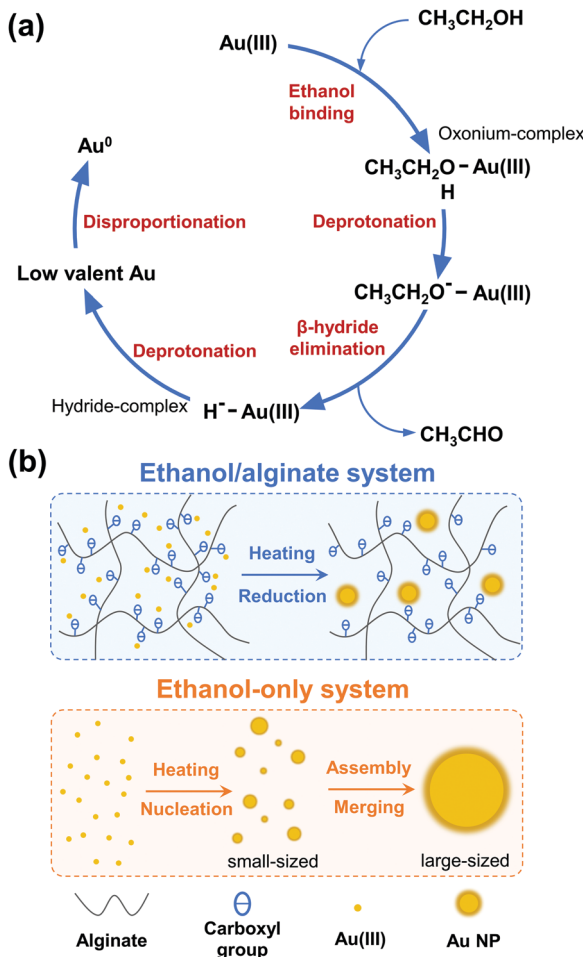
NPs, the appearance of a new band at 1730 cm⁻¹ indicates the presence of a six-membered cyclic ketone, revealing a process by which the -OH groups underwent oxidation to C=O during the reaction.⁷³

Generally, sodium alginate itself can function as a reducing agent for nanoparticle preparation.⁷³⁻⁷⁵ To confirm the role of sodium alginate in the ethanol/alginate system, additional experiments were conducted by synthesizing Au NPs in the alginate-only solution under the same conditions. As shown in Fig. S9, (ESI†) the alginate-only system also lacked efficiency. For the Au NPs synthesized in the 1% w/v alginate aqueous solutions, the reaction required a long reaction time (more than 2 h). When the concentration decreased to 0.5% w/v, the weakened absorbance compared to the 1% w/v group implied only some Au(III) was reduced. Au NPs could not even form in a 0.1% w/v alginate aqueous solution. Given the weaker reducing capacity of sodium alginate and its lower concentration, ethanol is considered to play a leading role in the ethanol/alginate system where Au(III) was reduced with the oxidation of ethanol to aldehyde and carboxylic acid (Scheme 1(a)).^{47,48,76} Ethanol initially coordinates to Au(III) to generate an oxonium-complex. The resulting oxonium-complex would lose a proton and yield an ethoxide-complex. Subsequent β -hydride elimination generates the hydride-complex, which then undergoes further deprotonation to yield a low valent Au ion and is eventually reduced to a zero-valent state through disproportionation. In general, the reduction of Au(0) from Au(III) accompanies the oxidation of ethanol into acetaldehyde, and the formation of acetaldehyde during the process is supported by the studies of Hirai *et al.*, in which the formation of acetaldehyde was detected by gas-liquid partition chromatography (GLPC)⁴⁸ and chromotropic acid-sulfuric acid methods,⁴⁹ respectively. The reaction equation is shown below.



As a supplementary role, sodium alginate provided carboxy anions and extra reducing groups to the ethanol system. As illustrated in Scheme 1(b), Au(III) could be evenly dispersed in ethanol/alginate solution by chelating gold chloride anionic complexes with oxygen atoms from carboxyl and hydroxyl groups of alginate.⁷⁷ The addition of sodium alginate increased the number of groups involved in the reaction (Fig. 9(e)), which enhanced the reducing capacity of the ethanol system and promoted the reduction rate of Au(III) to Au(0). Meanwhile, due to the high reduction rate, a larger number of nuclei would be generated, which caused the formation of Au NPs with smaller sizes.⁷⁸ Therefore, the high nucleation probability in this highly reductive system is another factor that can control the size of synthesized Au NPs in addition to the alginate chain-formed cavities. In contrast, in the ethanol-only system, due to the longer reaction time, small particles shrank and disappeared, while large particles absorbed the atoms from the smaller dissolving particles and continued growing, which followed the Ostwald ripening model.⁷⁹ As a result of the lack of stabilizing and capping agents, the assembly and merging between Au NPs were inevitable, and large-sized Au NPs formed consequently.^{80,81}

3.2.3. Injectability of alg-Au NPs. In the synthesis process, the ratios of Au NPs to sodium alginate were fixed. Since the Au NP amount is critical to the imaging capability, a higher amount of Au NPs could provide a better imaging quality. Paradoxically, a higher Au NP amount would be accompanied by more sodium alginate, which would lead to an increased extraction force during the injection (Fig. 3). Therefore, removal of sodium alginate while maintaining the properties of Au NPs (*e.g.*, size and dispersibility) is necessary before injectability



Scheme 1 Schematic illustration of the (a) ethanol reduction method and (b) formation process of Au NPs in the ethanol/alginate and ethanol-only system.

measurement. As sodium alginate can be decomposed at a high temperature,⁸² sodium alginate was removed by thermal treatment in this work. Based on the sodium alginate decomposition behaviour at different temperatures, the thermal treatment temperature was set at 400 °C because higher temperatures (600 °C) would cause the sintering between Au NPs (Fig. S10, ESI†). In Fig. S11, (ESI†) from the TEM images, it is evident that the morphology of the Au NPs did not change significantly after thermal treatment. A few large-sized Au NPs could also be observed due to the sintering caused by the high temperature, which led to a slight increase in the average size. However, the amount of sintered Au NPs and the increased average size are negligible and acceptable. By comparing the TG curves before and after the thermal treatment, there was essentially no weight loss after the treatment, confirming the effective removal of sodium alginate *via* thermal treatment.

After the synthesis of alg-Au NPs and the removal of excess sodium alginate, the injectability of alg-Au NPs was studied with the optimal injection conditions in Section 3.1.2, in which the injection medium concentration was 2.5% w/v and the Au NP concentration was 0.5 g mL⁻¹. As shown in Fig. 10, the

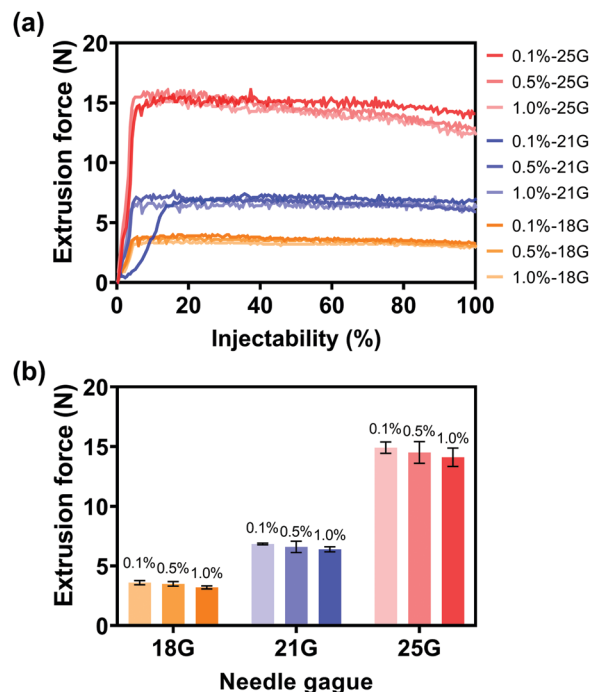


Fig. 10 (a) Extrusion force curves and (b) average extrusion force of alg-Au NPs synthesized in different alginate concentrations through different needles.

average extrusion forces required for Au NPs synthesized with different concentrations of alginate to pass through different gauge needles were: 3.5, 3.6, and 3.2 N for 18 G needles (inner diameter: 0.84 mm); 6.9, 6.6, and 6.4 N for 21 G needles (inner diameter: 0.51 mm); and 14.9, 14.5, and 14.1 N for 25 G needles (inner diameter: 0.26 mm). As mentioned in Section 3.1.2, a portion of the extrusion force is responsible for forcing the injection medium through the needle, accounting for needles with smaller inner diameters requiring larger extrusion forces. However, all extrusion forces are less than 50 N, which is extremely user-friendly for the surgeon during surgery. It is also worth noting that the alg-Au NPs synthesized in 0.1, 0.5, and 1.0% w/v alginate aqueous solutions with average sizes of 21.8 ± 5.1 , 18.2 ± 3.0 , and 14.1 ± 3.5 nm can all pass through different gauge needles, and even the injectability through the 25 G needle was also 100%. These results suggest that the injectability of Au NPs had been significantly improved by controlling the size of Au NPs with the addition of sodium alginate.

3.2.4. Imaging performance. Fig. 11(a) shows X-ray visualization test images of alg-Au NPs and the pattern matching scores are displayed in Table S2 and Fig. S12 (ESI†). The amounts of gold contained in the samples were calculated based on their TG analysis, as shown in Fig. S13 (ESI†). Since the size difference between alg-Au NPs was not significant (14.1 to 21.8 nm) compared to Au NPs synthesized in the ethanol-only system (242.5 nm), the normalized pattern matching scores (Fig. 11(b)) reveal that the gold amount, rather than the average size, was the major factor in determining the imaging capability. However, the alg-Au NPs with smaller sizes



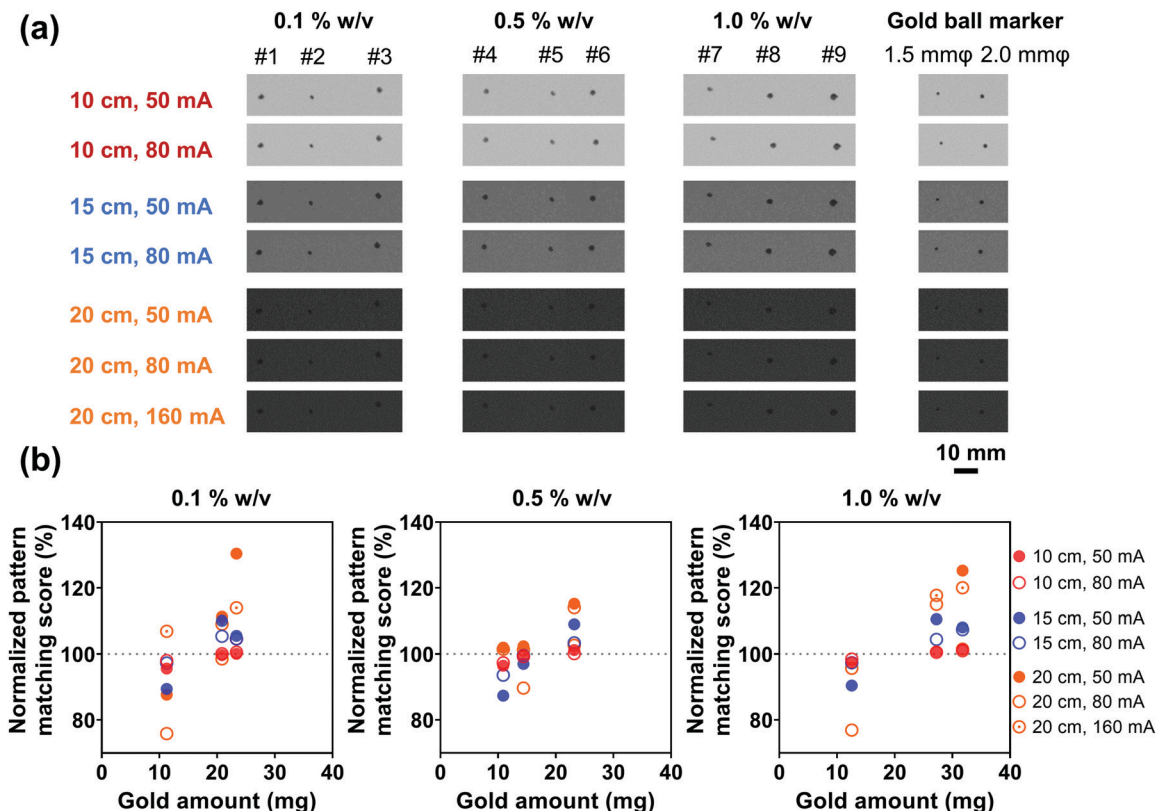


Fig. 11 (a) X-Ray visualization image of alg-Au NPs and gold ball markers under different acrylic resin thicknesses and tube currents. (b) Relationship between normalized pattern matching scores and different gold amounts.

showed higher normalized pattern matching scores (over 100%) with a lower gold amount (about 20 mg). This can be attributed to the increased surface area with the decrease in size. With the same gold concentration, smaller Au NPs could offer a larger gold surface area. Since the X-ray attenuation is target area dependent, small Au NPs with a larger surface area would exhibit more dramatic X-ray attenuation.^{70,83} Meanwhile, the smaller size implied that a large number of Au NPs would distribute in the path of X-ray transmission, which increased the absorption or deflection (scatter) of photons and eventually led to X-ray attenuation as well.⁸⁴

4. Conclusions

In summary, Au NPs designed as injectable fiducial markers for RGPT were synthesized *via* ethanol-only and ethanol/alginate systems, respectively. Their injectability and imaging capabilities as fiducial markers were evaluated. Within the range of parameters studied, the injection medium viscosity, Au NP concentration, and needle gauge were found to be the major factors that would affect their injectability, while the gold amount and particle size dominated their imaging performance. Compared to conventional gold ball markers (1.5 or 2.0 mm φ), Au NPs prepared in the ethanol-only system had an improved injectability (through 18 G and 21 G needles) and an almost identical imaging capability. This work also

reported a novel reducing system based on the mixture of ethanol and alginate. The addition of alginate into the ethanol reduction system can improve the reaction efficiency, control the size of synthesized Au NPs, and prevent aggregation between Au NPs. As an anionic polymer with a high charge density, alginate can significantly enhance the reducing capacity of the ethanol system and control the size of alg-Au NPs through the formed cavities and the increased nucleation probability. Due to the size control during synthesis, the alg-Au NPs with smaller sizes (14.1 to 21.8 nm) exhibited a superior injectability, up to 100% even through 25 G needles with an extrusion force less than 17 N, especially for the injection of high-concentration Au NPs. The better imaging capability of alg-Au NPs was also verified in the X-ray visualization test. Though the imaging performance of Au NPs and alg-Au NPs as fiducial markers has been examined and confirmed after injection, future follow-up studies should be systematically explored by investigating the cytotoxicity and *in vivo* imaging performance of alg-Au NPs, the reaction mechanism underlying the monitoring of transition from ethanol to acetaldehyde as well as the role of sodium alginate in the process, and the feasibility of the ethanol/alginate system in the synthesis of other metal nanoparticles. Altogether, this work provides a fresh perspective on the green and high-efficiency synthesis strategy of Au NPs without the introduction of toxic reducing, capping, or stabilizing agents and their applications as a fiducial marker for RGPT.

Author contributions

H. L. performed the experiments, collected, and analyzed the data, and wrote the draft. M. T. N. assisted in the experiments and helped with the analysis. N. M. performed X-ray visualization test and analyzed the obtained data. H. S. and T. Y. conceived the idea. T. Y. directed and supervised the research. The manuscript was written through the contributions of all authors. All authors have approved the final version of the manuscript.

Conflicts of interest

There are no conflicts to declare.

Acknowledgements

This work was partially supported by Hokkaido University. This work was also supported in part by The Translational Research program; Strategic Promotion for practical application of Innovative medical Technology (TR-SPRINT) funded by The Japan Agency for Medical Research and Development (AMED) and by Grants-in-Aid for Regional R&D Proposal-Based Program from Northern Advancement Centre for Science and Technology (NOASTEC), Hokkaido, Japan. TY thanks the JKA Foundation (Promotion fund from KEIRIN RACE: 2021-M113) for the partial financial support. The authors thank Dr Y. Ishida, Dr S. Zhu, and Mr H. Tsukamoto (Hokkaido University) for fruitful discussions and experimental assistance. The authors thank Mr T. Tanioka and Ms R. Yokohira (Hokkaido University) for their assistance in the TEM analysis. The authors gratefully acknowledge Hokkaido University Hospital Clinical Research and Medical Innovation Centre for the fruitful discussions and the technical assistances. We also thank the Central Institute of Isotope Science (CIS), Hokkaido University for assistance with the X-ray visualization tests. H.L. would like to thank the China Scholarship Council (CSC) for the financial support of his work in Sapporo.

Notes and references

- 1 M. Xu, M. G. Soliman, X. Sun, B. Pelaz, N. Feliu, W. J. Parak and S. Liu, *ACS Nano*, 2018, **12**, 10104–10113.
- 2 P. Si, N. Razmi, O. Nur, S. Solanki, C. M. Pandey, R. K. Gupta, B. D. Malhotra, M. Willander and A. de la Zerda, *Nanoscale Adv.*, 2021, **3**, 2679–2698.
- 3 H. Liu, K. Ikeda, M. T. Nguyen, S. Sato, N. Matsuda, H. Tsukamoto, T. Tokunaga and T. Yonezawa, *ACS Omega*, 2022, **2022**(7), 6238–6247.
- 4 Z. Gao, H. Ye, D. Tang, J. Tao, S. Habibi, A. Minerick, D. Tang and X. Xia, *Nano Lett.*, 2017, **17**, 5572–5579.
- 5 X. Bai, Y. Wang, Z. Song, Y. Feng, Y. Chen, D. Zhang and L. Feng, *Int. J. Mol. Sci.*, 2020, **21**, 2480.
- 6 W. Sun, L. Luo, Y. Feng, Y. Cai, Y. Zhuang, R. J. Xie, X. Chen and H. Chen, *Angew. Chem., Int. Ed.*, 2020, **59**, 9914–9921.
- 7 R. S. Riley and E. S. Day, *Wiley Interdiscip. Rev.: Nanomed. Nanobiotechnol.*, 2017, **9**, e1449.
- 8 S. Han, W. Liu, M. Zheng and R. Wang, *Anal. Chem.*, 2020, **92**, 4780–4787.
- 9 Y. Liu, B. M. Crawford and T. Vo-Dinh, *Immunotherapy*, 2018, **10**, 1175–1188.
- 10 D. Zhang, T. Wu, X. Qin, Q. Qiao, L. Shang, Q. Song, C. Yang and Z. Zhang, *Nano Lett.*, 2019, **19**, 6635–6646.
- 11 R. Popovtzer, A. Agrawal, N. A. Kotov, A. Popovtzer, J. Balter, T. E. Carey and R. Kopelman, *Nano Lett.*, 2008, **8**, 4593–4596.
- 12 K. Ikeda, H. Liu, N. Miyamoto, M. T. Nguyen, H. Shirato and T. Yonezawa, *ACS Appl. Bio Mater.*, 2022, **5**, 1259–1266.
- 13 A. R. Montazerabadi, M. A. Oghabian, R. Irajirad, S. Muhammadnejad, D. Ahmadvand, H. Delavari and S. R. Mahdavi, *NANO*, 2015, **10**, 1550048.
- 14 S. B. Lee, S. W. Lee, S. Y. Jeong, G. Yoon, S. J. Cho, S. K. Kim, I. K. Lee, B.-C. Ahn, J. Lee and Y. H. Jeon, *ACS Appl. Mater. Interfaces*, 2017, **9**, 8480–8489.
- 15 Y. Wu, M. R. Ali, K. Chen, N. Fang and M. A. El-Sayed, *Nano Today*, 2019, **24**, 120–140.
- 16 T. Kim, Q. Zhang, J. Li, L. Zhang and J. V. Jokerst, *ACS Nano*, 2018, **12**, 5615–5625.
- 17 T. Kanehira, T. Matsuura, S. Takao, Y. Matsuzaki, Y. Fujii, T. Fujii, Y. M. Ito, N. Miyamoto, T. Inoue and N. Katoh, *Int. J. Radiat. Oncol. Biol. Phys.*, 2017, **97**, 173–181.
- 18 T. Matsuura, K. Maeda, K. Sutherland, T. Takayanagi, S. Shimizu, S. Takao, N. Miyamoto, H. Nihongi, C. Toramatsu and Y. Nagamine, *Med. Phys.*, 2012, **39**, 5584–5591.
- 19 S. Shimizu, T. Matsuura, M. Umezawa, K. Hiramoto, N. Miyamoto, K. Umegaki and H. Shirato, *Phys. Med.*, 2014, **30**, 555–558.
- 20 M. Machiels, J. van Hooft, P. Jin, M. I. van Berge Henegouwen, H. M. van Laarhoven, T. Alderliesten and M. C. Hulshof, *Gastrointest. Endosc.*, 2015, **82**, 641–649.
- 21 N. Bhagat, N. Fidelman, J. C. Durack, J. Collins, R. L. Gordon, J. M. LaBerge and R. K. Kerlan, *Cardiovasc. Intervent. Radiol.*, 2010, **33**, 1186–1191.
- 22 Z. Fawaz, M. Yassa, D. Nguyen and P. Vavassis, *Cancer Radiother.*, 2014, **18**, 736–739.
- 23 G. Maiorano, E. Mele, M. Frassanito, E. Restini, A. Athanassiou and P. Pompa, *Nanoscale*, 2016, **8**, 18921–18927.
- 24 S. Mohammadian, J. Fokkema, A. V. Agronskaia, N. Liv, C. de Heus, E. van Donselaar, G. A. Blab, J. Klumperman and H. C. Gerritsen, *Sci. Rep.*, 2019, **9**, 1–10.
- 25 J. D. Trono, K. Mizuno, N. Yusa, T. Matsukawa, K. Yokoyama and M. Uesaka, *J. Radiat. Res.*, 2011, **52**, 103–109.
- 26 A. Menazea and M. Ahmed, *J. Mol. Struct.*, 2020, **1217**, 128401.
- 27 L. Torrisi and A. Torrisi, *Radiat. Eff. Defects Solids*, 2018, **173**, 729–739.
- 28 Y. Hatakeyama, K. Onishi and K. Nishikawa, *RSC Adv.*, 2011, **1**, 1815–1821.
- 29 Y. Shang, C. Min, J. Hu, T. Wang, H. Liu and Y. Hu, *Solid State Sci.*, 2013, **15**, 17–23.
- 30 A. Lähde, I. Koshevoy, T. Karhunen, T. Torvela, T. A. Pakkanen and J. Jokiniemi, *J. Nanopart. Res.*, 2014, **16**, 1–8.
- 31 C. M. Müller, F. C.-F. Mornaghini and R. Spolenak, *Nanotechnology*, 2008, **19**, 485306.



32 P. Iqbal, J. A. Preece and P. M. Mendes, Nanotechnology: The “Top – Down” and “Bottom – Up” Approaches, in *Supramolecular chemistry: from molecules to nanomaterials*, Wiley-VCH, 2012, DOI: [10.1002/9780470661345.smc195](https://doi.org/10.1002/9780470661345.smc195).

33 T. Yonezawa, S. Zhu and M. T. Nguyen, Miscellaneous Reductants, in *Reducing Agents in Colloidal Nanoparticle Synthesis*, ed. S. Moudrikoudis, RSC Publishing, 2021, pp. 393–459, DOI: [10.1039/9781839163623-00393](https://doi.org/10.1039/9781839163623-00393).

34 J. Kimling, M. Maier, B. Okenve, V. Kotaidis, H. Ballot and A. Plech, *J. Phys. Chem. B*, 2006, **110**, 15700–15707.

35 S. Kumar, K. Gandhi and R. Kumar, *Ind. Eng. Chem. Res.*, 2007, **46**, 3128–3136.

36 E. Agunloye, L. Panariello, A. Gavriilidis and L. Mazzei, *Chem. Eng. Sci.*, 2018, **191**, 318–331.

37 N. Wangoo, K. Bhasin, S. Mehta and C. R. Suri, *J. Colloid Interface Sci.*, 2008, **323**, 247–254.

38 K. Sun, J. Qiu, J. Liu and Y. Miao, *J. Mater. Sci.*, 2009, **44**, 754–758.

39 M. Brust, M. Walker, D. Bethell, D. J. Schiffrin and R. Whyman, *J. Chem. Soc., Chem. Commun.*, 1994, 801–802.

40 T. Yonezawa, K. Yasui and N. Kimizuka, *Langmuir*, 2001, **17**, 271–273.

41 D. L. Xia, Y. F. Wang, N. Bao, H. He, X. D. Li, Y. P. Chen and H. Y. Gu, *Appl. Biochem. Biotechnol.*, 2014, **174**, 2458–2470.

42 C. Uboldi, D. Bonacchi, G. Lorenzi, M. Hermanns, C. Pohl, G. Baldi, R. E. Unger and C. J. Kirkpatrick, *Part. Fibre Toxicol.*, 2009, **6**, 1–12.

43 C. Freese, C. Uboldi, M. I. Gibson, R. E. Unger, B. B. Weksler, I. A. Romero, P. O. Couraud and C. J. Kirkpatrick, *Part. Fibre Toxicol.*, 2012, **9**, 1–11.

44 T. Niidome, M. Yamagata, Y. Okamoto, Y. Akiyama, H. Takahashi, T. Kawano, Y. Katayama and Y. Niidome, *J. Controlled Release*, 2006, **114**, 343–347.

45 S. Liu and M. Han, *Adv. Funct. Mater.*, 2005, **15**, 961–967.

46 M. H. Hussain, N. F.-A. Bakar, A. N. Mustapa, K. F. Low, N. H. Othman and F. Adam, *Nanoscale Res. Lett.*, 2020, **15**, 1–10.

47 H. Hirai, H. Chawanya and N. Toshima, *React. Polym.*, 1985, **3**, 127–141.

48 H. Hirai, Y. Nakao and N. Toshima, *J. Macromol. Sci., Chem.*, 1979, **13**, 727–750.

49 H. Hirai, Y. Nakao, N. Toshima and K. Adachi, *Chem. Lett.*, 1976, 905–910.

50 N. Toshima, K. Kushihashi, T. Yonezawa and H. Hirai, *Chem. Lett.*, 1989, 1769–1772.

51 N. Toshima, T. Yonezawa and K. Kushihashi, *J. Chem. Soc., Faraday Trans.*, 1993, **89**, 2537–2543.

52 T. Yonezawa and N. Toshima, *J. Chem. Soc., Faraday Trans.*, 1995, **91**, 4111–4119.

53 X. Zhao, Y. Xia, Q. Li, X. Ma, F. Quan, C. Geng and Z. Han, *Colloids Surf., A*, 2014, **444**, 180–188.

54 H. Shirato, S. Shimizu, T. Kunieda, K. Kitamura, M. Herk, K. Kagei, T. Nishioka, S. Hashimoto, K. Fujita, H. Aoyama, K. Tsuchiya, K. Kudo and K. Miyasaka, *Int. J. Radiat. Oncol. Biol. Phys.*, 2000, **48**, 1187–1195.

55 M.-d P. Caldas, F. M.-d M. Ramos-Perez, S. M.-d Almeida and F. Haiteir-Neto, *J. Appl. Oral Sci.*, 2010, **18**, 264–267.

56 N. Miyamoto, M. Ishikawa, G. Bengua, K. Sutherland, R. Suzuki, S. Kimura, S. Shimizu, R. Onimaru and H. Shirato, *Phys. Med. Biol.*, 2011, **56**, 4803.

57 Y. Q. He, S. P. Liu, L. Kong and Z. F. Liu, *Spectrochim. Acta, Part A*, 2005, **61**, 2861–2866.

58 D. M. Hariyadi and N. Islam, *Adv. Pharmacol. Pharm. Sci.*, 2020, 8886095.

59 F. Cilurzo, F. Selmin, P. Minghetti, M. Adami, E. Bertoni, S. Lauria and L. Montanari, *AAPS PharmSciTech*, 2011, **12**, 604–609.

60 A. Allahham, D. Mainwaring, P. Stewart and J. Marriott, *J. Pharm. Pharmacol.*, 2004, **56**, 709–716.

61 J. J. Hung, A. U. Borwankar, B. J. Dear, T. M. Truskett and K. P. Johnston, *J. Membr. Sci.*, 2016, **508**, 113–126.

62 V. Jayaprakash, M. Costalanga, S. Dhulipala and K. K. Varanasi, *Adv. Healthcare Mater.*, 2020, **9**, 2001022.

63 P. Raveendran, J. Fu and S. L. Wallen, *Green Chem.*, 2006, **8**, 34–38.

64 G. Sonavane, K. Tomoda and K. Makino, *Colloids Surf., B*, 2008, **66**, 274–280.

65 W. Cho, M. Cho, J. Jeong, M. Choi, B. Han, H. Shin, J. Hong, B. Chung, J. Jeong and M. Cho, *Toxicol. Appl. Pharmacol.*, 2010, **245**, 116–123.

66 G. Sonavane, K. Tomoda, A. Sano, H. Ohshima, H. Terada and K. Makino, *Colloids Surf., B*, 2008, **65**, 1–10.

67 T. Mironava, M. Hadjriargyrou, M. Simon, V. Jurukovski and M. H. Rafailovich, *Nanotoxicology*, 2010, **4**, 120–137.

68 B. D. Chithrani and W. C. Chan, *Nano Lett.*, 2007, **7**, 1542–1550.

69 X. D. Zhang, D. Wu, X. Shen, J. Chen, Y. M. Sun, P. X. Liu and X. J. Liang, *Biomaterials*, 2012, **33**, 6408–6419.

70 C. Xu, G. A. Tung and S. Sun, *Chem. Mater.*, 2008, **20**, 4167–4169.

71 E. C. Dreaden, L. A. Austin, M. A. Mackey and M. A. El-Sayed, *Ther. Deliv.*, 2012, **3**, 457–478.

72 S. Lopes, L. Bueno, F. D. Aguiar Junior and C. Finkler, *An. Acad. Bras. Cienc.*, 2017, **89**, 1601–1613.

73 J. Yang and J. Pan, *Acta Mater.*, 2012, **60**, 4753–4758.

74 S. K. Balavandy, K. Shameli and Z. Z. Abidin, *Int. J. Electrochem. Sci.*, 2015, **10**, 486–497.

75 M. Zahran, H. B. Ahmed and M. El-Rafie, *Carbohydr. Polym.*, 2014, **111**, 10–17.

76 O. Levy-Ontman, E. Stamker and A. Wolfson, *Metals*, 2021, **11**, 1443.

77 X. Gao, Y. Zhang and Y. Zhao, *Carbohydr. Polym.*, 2017, **159**, 108–115.

78 G. Frens, *Nat. Phys. Sci.*, 1973, **241**, 20–22.

79 N. G. Bastús, J. Comenge and V. Puntes, *Langmuir*, 2011, **27**, 11098–11105.

80 B. Jin, M. L. Sushko, Z. Liu, C. Jin and R. Tang, *Nano Lett.*, 2018, **18**, 6551–6556.

81 Z. Aabdin, J. Lu, X. Zhu, U. Anand, N. D. Loh, H. Su and U. Mirsaidov, *Nano Lett.*, 2014, **14**, 6639–6643.

82 J. Soares, J. Santos, G. Chierice and E. Cavalheiro, *Eclética Quím.*, 2004, **29**, 57–64.

83 Z. Wang, L. Wu and W. Cai, *Chem. – Eur. J.*, 2010, **16**, 1459–1463.

84 M. H. McKetty, *Radiographics*, 1998, **18**, 151–163.

